

# Chapter 3

## Gas Seepage Detection and Gas Migration Mechanisms



Kun Zhang, Haibin Song, Jiangxin Chen, Minghui Geng, and Boran Liu

**Abstract** Gas seepages are often observed at the seafloor and can form cold seep systems, which are important for climate change, geohazards, and biogeochemical cycles. Many kinds of methods have been used to detect gas seepages, e.g., video imaging, active acoustic, passive acoustic, and direct gas sampling. In this chapter, we introduce the characteristics of these methods and show their applications in the South China Sea (SCS). Particle image velocimetry (PIV) technology is used here to quantitatively detect gas seepage in the northwestern SCS and visualize the seepage flow field. The gas migration mechanisms are also discussed. With the development of technologies, long-term, three-dimensional, and comprehensive observations is permitted to quantitatively characterize gas seepages, which can help us understand the formation and mechanism of gas seepages further in the future. Physical and numerical simulations of gas migration and geohazard processes would also be helpful in the future for understanding the fate of gas seepages.

---

K. Zhang · H. Song (✉)

State Key Laboratory of Marine Geology, School of Ocean and Earth Science, Tongji University, Shanghai 20092, China  
e-mail: [hbsong@tongji.edu.cn](mailto:hbsong@tongji.edu.cn)

K. Zhang

e-mail: [kunzhang@tongji.edu.cn](mailto:kunzhang@tongji.edu.cn)

J. Chen

Key Laboratory of Gas Hydrate, Ministry of Natural Resources, Qingdao Institute of Marine Geology, Qingdao 266071, China  
e-mail: [jiangxin\\_chen@sina.com](mailto:jiangxin_chen@sina.com)

M. Geng

Key Laboratory of Marine Mineral Resources, Ministry of Natural Resources, Guangzhou Marine Geological Survey, Guangzhou 510760, China  
e-mail: [gengminghui5591788@163.com](mailto:gengminghui5591788@163.com)

B. Liu

Laboratory of Coastal and Marine Geology, Ministry of Natural Resources, Third Institute of Oceanography, Xiamen 361005, China  
e-mail: [liuboran@tio.org.cn](mailto:liuboran@tio.org.cn)

© The Author(s) 2023

D. Chen and D. Feng (eds.), *South China Sea Seeps*,  
[https://doi.org/10.1007/978-981-99-1494-4\\_3](https://doi.org/10.1007/978-981-99-1494-4_3)

## 3.1 Introduction

Gas seepage is a widely distributed geological feature around the world's oceans and lakes. It can transport larger amounts of natural gas (mainly methane) into the water column and even the atmosphere, which has been invoked as an important factor in climate change (Judd and Hovland 2007), submarine slope failures (Kvenvolden 1993), and biogeochemical cycles (Feng et al. 2010).

Gas seepages can not only influence the physical properties of the sediments near the seafloor but also significantly change the geomorphology of the seafloor, e.g., the formation of pockmarks, mud volcanoes, authigenic carbonates and cold seep biochemistry communities (Fig. 3.1). These features show different characteristics in geological, biogeochemical, and geophysical data (Judd and Hovland 2007), and many gas seepages have been detected in the South China Sea (SCS) through these features. Most of the gas seepages are located in the water depth range of 200–3000 m in the northern SCS, e.g., Southwest Taiwan Island, Dongsha Uplift, and Qiongdongnan Basin. Haima and Site F are the most famous and well-studied active cold seep areas in the SCS (Fig. 3.2). The geomorphological properties, subsurface structures, and water column characteristics of gas seepages have been studied and summarized to show the features and mechanisms in the SCS (Feng et al. 2018), and some quantitative studies have also attempted to show the fate and effect of these seepages (Di et al. 2020).

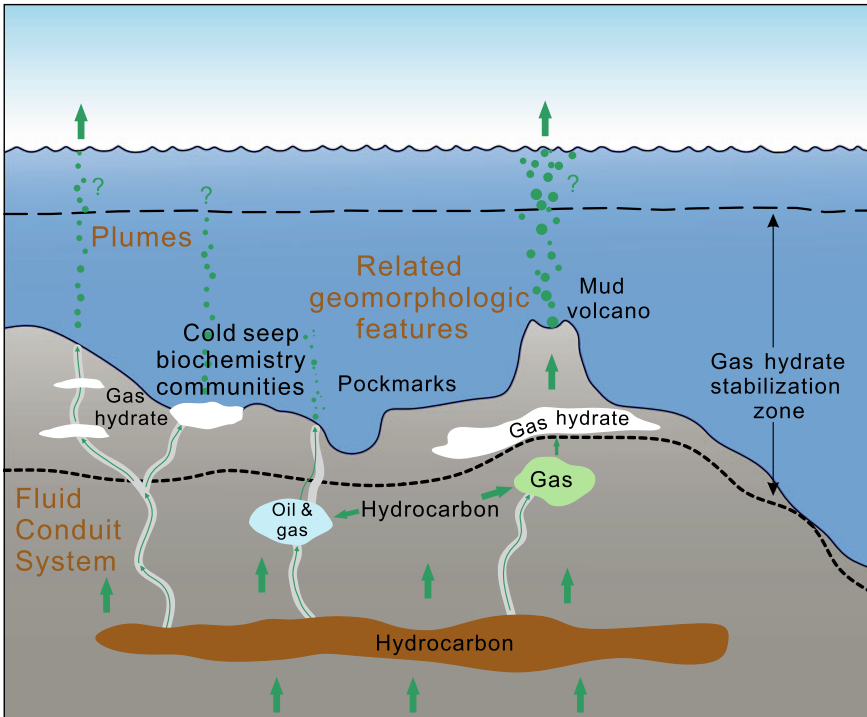
In this chapter, we first introduce the progress of gas seepage detection in the SCS and then demonstrate the methods for the quantitative characterization of gas seepage. Subsequently, gas migration mechanisms are discussed. Finally, we provide some ideas for detecting gas seepages and studying gas migration mechanisms.

## 3.2 Detecting Gas Seepage in the South China Sea

### 3.2.1 Bubbles

The bubbles emitted from gas seepages are the most significant characteristic of gas seepages. Because gas bubbles induce a strong change in acoustic impedance, they can be detected in acoustic water column data by their typical “flare” shape or as rising lines when single bubbles/bubble clouds are emitted (Urban et al. 2017).

Gas plumes have been identified for their significant “flare” shape on multibeam echosounder system (MBES) water column images (Fig. 3.3) in offshore SW Taiwan Island (Hsu et al. 2013, 2018a), the Pearl River Mouth Basin (Zhu et al. 2018), and the Qiongdongnan Basin (Yang et al. 2018; Wei et al. 2020; Liu et al. 2021). The gas plumes in these regions have significant spatiotemporal variations. The heights of the plumes range from tens of meters to over 750 m, some of which are higher than the upper boundary of the Gas Hydrate Stability Zone (GHSZ) in the Qiongdongnan Basin. The hydrated skin of bubbles may extend the lifetime of gas bubbles and cause



**Fig. 3.1** Main elements of gas seepages (modified from *Marine and Petroleum Geology*, 22(4), Whelan et al. Surface and subsurface manifestations of gas movement through a N–S transect of the Gulf of Mexico Sea, 479–497. Copyright (2005), with permission from Elsevier)

the gas plumes to reach higher (Liu et al. 2021). The shapes of these plume usually vary with time due to the bottom current (Liu et al. 2021). Ocean tides may also influence the strength of gas seepages and cause emission tremors (Hsu et al. 2013). Due to periodic variations in subsurface pressure, the locations of gas emission points are not fixed, and gas flux is unstable in the Qiongdongnan Basin (Wei et al. 2020).

Gas bubbles also show unique features on water column images of the chirp subbottom system and multichannel seismic system (Xu et al. 2012; Liu et al. 2015; Chen et al. 2017, 2020). Liu et al. (2015) identified an acoustic plume on subbottom water column images in the northeast SCS, and they suspected that this plume was caused by gas seepage (Fig. 3.4). Acoustic turbidity, acoustic curtain, acoustic blanket, and enhanced reflection were identified on subbottom profiles and considered to be indicators of shallow gas below the seafloor. On seismic sections of the water column, bubble plumes are characteristic of staggered boundary events, strong amplitude, and high frequency (Chen et al. 2017, 2020). For example, Chen et al. (2017) processed the multichannel seismic data near the Dongsha uplift and the northern Zhongjiannan Basin using seismic oceanography methods. Their analysis

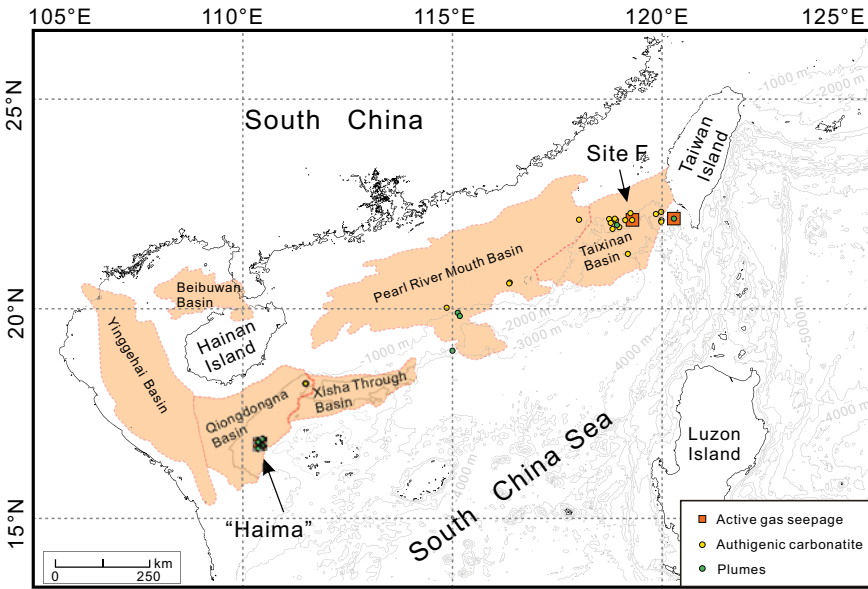


Fig. 3.2 Gas seepages in the Northern South China Sea

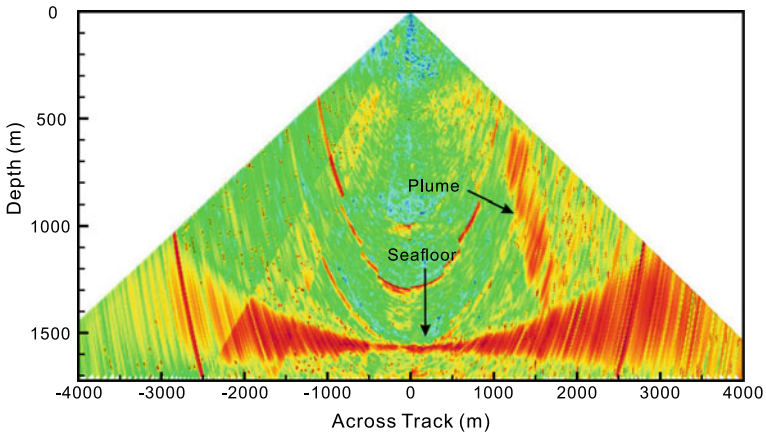
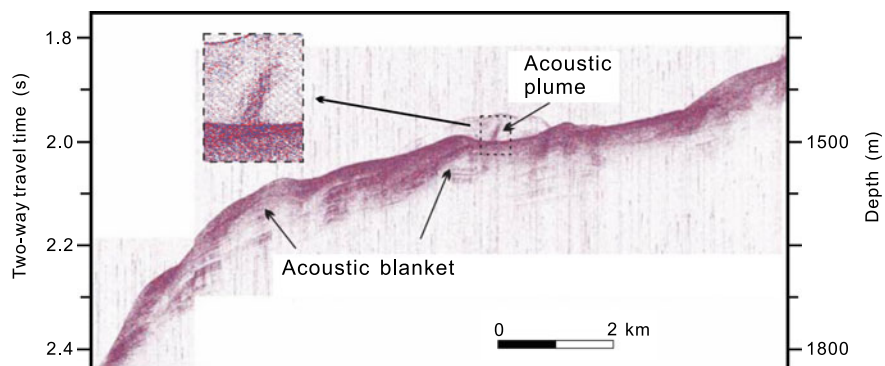
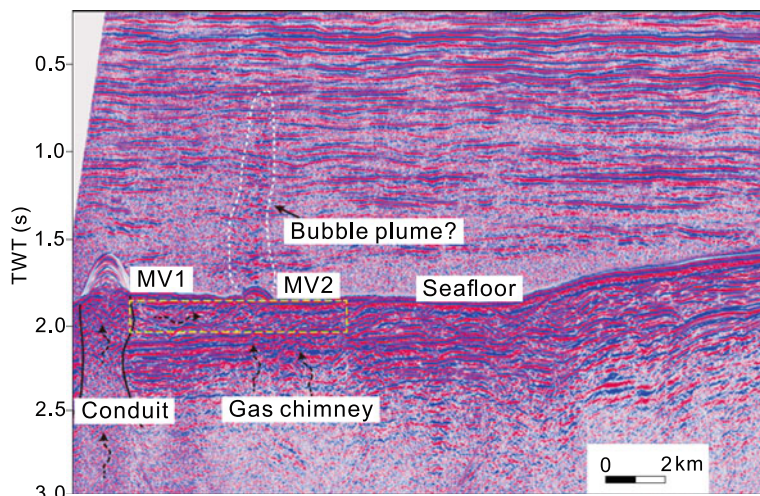


Fig. 3.3 Multibeam Echosounder Systems water column images. The flare shape reflection indicates the gas seepage

showed that gas seepages primarily present plume, broom, and/or irregular shapes that have weak and chaotic seismic reflections in the water column (Fig. 3.5).



**Fig. 3.4** Acoustic plume and blanket on chirp subbottom profiles (redrawn from Chinese Journal of Geophysics-Chinese Edition, 58(1), Liu et al. Characteristics and formation mechanism of cold seep system in the northeastern continental slope of South China Sea from sub-bottom profiler data, 247–256. Copyright (2015), with permission from Science Press)



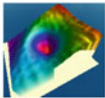
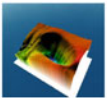
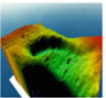
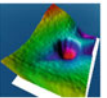

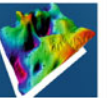
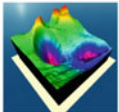
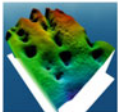
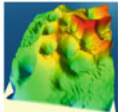
**Fig. 3.5** Possible bubble plumes in seismic sections of the water column, and mud volcanoes (MV) and gas chimneys in seismic sections of the sedimentary strata near the Dongsha uplift, northern South China Sea. (Reprinted from Chinese Journal of Geophysics-Chinese Edition, 60(2), Chen et al. A preliminary study of submarine cold seeps applying seismic oceanography techniques, 604–616. Copyright (2017), with permission from Science Press)

### 3.2.2 Pockmarks

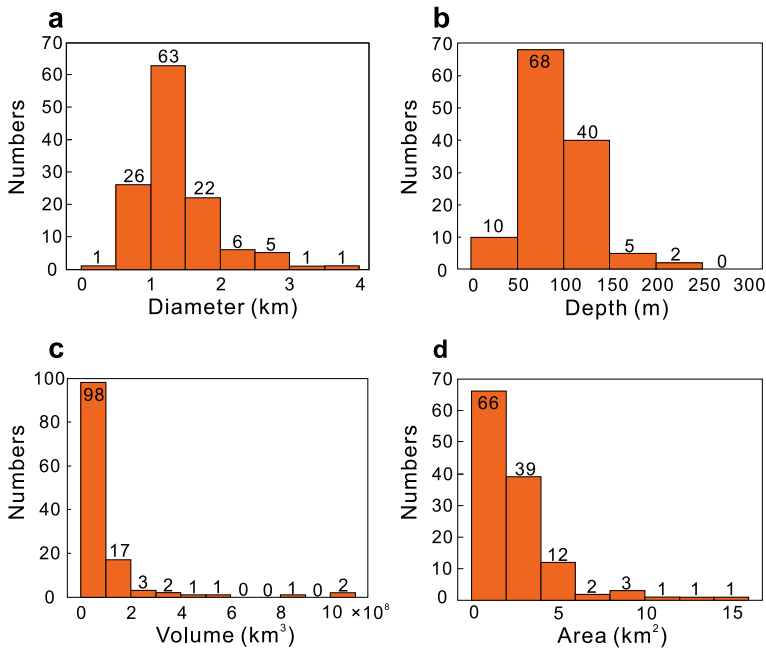
Pockmarks consist of depressions on the seafloor and are often considered to originate from fluid escape activities (Dandapath et al. 2010; Hovland et al. 2010). Different kinds of pockmarks have been discovered in the Taixinan Basin (Chen et al. 2010),

Pearl River mouth basin (Chen et al. 2015a; Zhu et al. 2020), Yinggehai Basin (Di et al. 2012), Qiongdongnan Basin (Bai et al. 2014; Wang et al. 2019), Xisha Massif (Sun et al. 2011; Luo et al. 2015), Zhongjiannan Basin (Chen et al. 2015a; Yu et al. 2021), Beikang Basin (Zhang et al. 2020a), and Reed Basin (Zhang et al. 2019; Zhu et al. 2020) of the northern, western, and southern margins of the SCS. According to the characteristics of pockmarks in the SCS, Chen et al. (2015b) proposed a general pockmark classification system based on three main pockmark characteristics: their shape, size, and composite pattern (Fig. 3.6). According to the geometrical shapes, pockmarks are classified as circular, elliptical, crescent, comet, elongated, and irregular pockmarks. By size, they can be classified as small pockmarks, normal pockmarks, giant pockmarks, and mega pockmarks, which have diameters on the order of several meters, tens of meters, hundreds of meters, and thousands of meters, respectively. A composite pattern describes how groups of pockmarks are organized. They can be classified as composites of pockmarks, pockmark strings, and pockmark groups.

Different geometrical parameters of pockmarks were also presented, e.g., diameter, depth, area, filled volume, and slopes (Fig. 3.7; Chen et al. 2015a; Zhang et al. 2020a). Many giant and mega pockmarks were found in the western and southern SCS margins, and the pockmarks reported in the northern SCS margin were relatively small. The diameter and depth of pockmarks usually have a positive correlation in the SCS (Chen et al. 2015a; Zhang et al. 2020a). However, the slopes and coefficients

Types	Circle	Elliptical	Crescent	Comet	Elongated	Irregular
3D View						
Types	Small		Normal	Gaint		Mega
Sizes	Several meters		Tens of meters	Hundreds of meters		Thousands of meters
Types	Composite		String		Group	
3D view						

**Fig. 3.6** Classification of pockmarks according to individual standard (modified from Deep Sea Research Part II: Topical Studies in Oceanography, 122, Chen et al. Morphologies, classification and genesis of pockmarks, mud volcanoes and associated fluid escape features in the northern Zhongjiannan Basin, South China Sea, 106–117. Copyright (2015), with permission from Elsevier, and Marine Geophysical Research, 41(2), Zhang et al. A preliminary study on morphology and genesis of giant and mega pockmarks near Andu Seamount, Nansha Region (South China Sea), 1–12. Copyright (2015), with permission from Springer Nature)



**Fig. 3.7** Histograms and rose diagram of morphological parameters of pockmarks in the Beikang Basin, southern South China Sea. **a** Diameter, **b** depth, **c** volume, and **d** surface area (modified from Marine Geophysical Research, 41(2), Zhang et al. A preliminary study on morphology and genesis of giant and mega pockmarks near Andu Seamount, Nansha Region (South China Sea), 1–12. Copyright (2015), with permission from Springer Nature)

of determination of the pockmark fitting curves are different in each area, showing a relatively poor linear relationship (Chen et al. 2015a).

High-angle faults, high-amplitude reflections, filled-up structures, and other fluid escape features are usually found beneath pockmarks (Sun et al. 2011; Zhang et al. 2020a). These underlying geological structures controls the formation and evolution of pockmarks (Gay et al. 2006). The seabed gradient, bottom currents, sediment types, and gas hydrate evolution also contribute to the development of pockmarks (Pilcher and Argents 2007; Dandapath et al. 2010; Bai et al. 2014; Sultan et al. 2014). In the western SCS, the development of pockmarks was found to be related to the formation of submarine channels (Chen et al. 2015b; Yu et al. 2021).

### 3.2.3 Mud Volcanoes

In contrast with pockmarks, mud volcanoes are positive geomorphological features on the seafloor and have flat, conical, or concave-down tops (Dupré et al. 2008; Ceramicola et al. 2018). Due to the rough seafloor and breccia deposits around mud



volcanoes, the acoustic backscatter strength near mud volcanoes is high (Chen and Song 2005). On chirp subbottom profiles, mud volcanoes show positive geomorphological features and acoustic blanket, acoustic turbidity, and enhanced reflections because of the clay, water, and gas inside the mud volcanoes (Schroot et al. 2005). On seismic profiles, weak reflections, chaotic reflections, and blank reflections are distributed inside mud volcanoes, and mud volcanoes also show positive relief (He et al. 2010; Wan et al. 2019).

Many mud volcanoes have been reported on the northern (Fig. 3.8) and western SCS margins (Chen et al. 2015a; Geng et al. 2019; Wan et al. 2019). The diameters of them are distributed between hundreds of meters and two kilometers, and their heights range from several meters to two hundred meters. Chen et al. (2015a) presented the statistical results on the relationship between the diameter and height of mud volcanoes in the northern and western margins of the SCS. They found that the mud volcanoes in individual areas showed good linear relationships, but all of them showed a relatively bad linear relationship. The classification of mud volcanoes is also diverse. Based on their morphology, structure, and kinetic characteristics, mud volcanoes are classified into deep source high-energy large-size mud volcanoes, shallow source-low energy-small mud volcanoes, budding mud volcanoes, canyon- and bottom current channel-related mud volcanoes, and pockmark- and gas chimney-related mud volcanoes in the western SCS margin (Wan et al. 2019). The formation mechanisms of mud volcanoes are distinct in different regions (Chen et al. 2015a), but the abundant sediments and overpressure usually provide the necessary conditions for the formation of mud volcanoes.

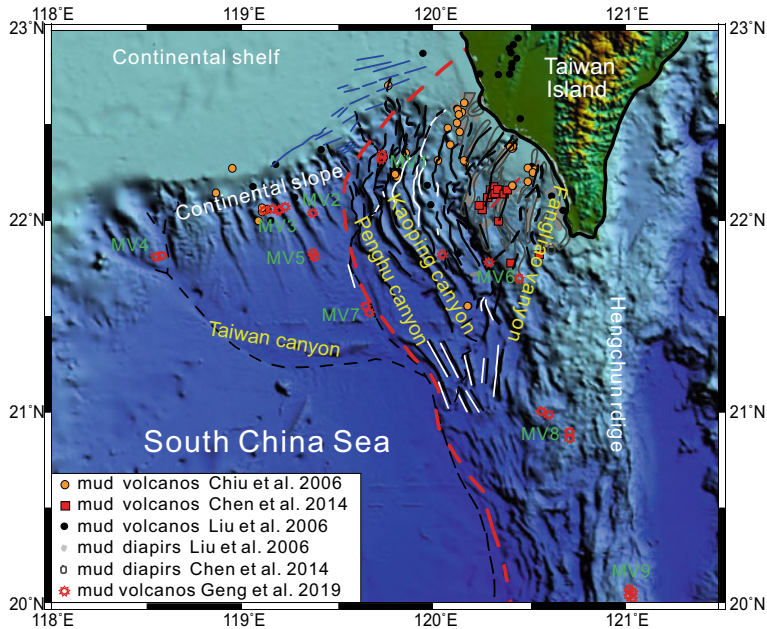
### ***3.2.4 Authigenic Carbonates***

The authigenic carbonates and chemosynthetic communities formed by gas seepages can change the acoustic impedance and roughness of the seafloor, which can be identified by enhanced backscatter on Sidescan Sonar Images (Chen and Song 2005; Dumke et al. 2014). For example, Site F is characterized by irregular and hummocky topography on a seabed relief map and by patches with high to medium backscatter intensities on side-scan sonar (Wang et al. 2021). On seismic and subbottom profiles, acoustic blanking usually appears beneath gas seepages because of acoustic shielding from carbonate rocks (Liu et al. 2015; Liu 2017).

### ***3.2.5 Subsurface Features Beneath a Gas Seepage***

Subsurface features connect a gas seepage at the seafloor with the source of gas in the subsurface layers and provide conduits for gas migration (Talukder 2012). High-angle faults, pipes, gas chimneys, mud diapirs, and bottom simulating reflections (BSRs) are often found beneath gas seepages (Sun et al. 2012, 2013; Wang et al. 2018a;





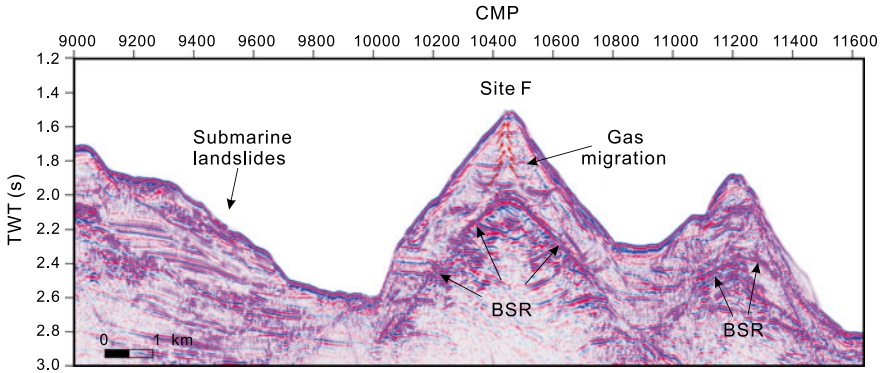
**Fig. 3.8** Mud volcanoes discovered in the northeastern South China Sea (modified from Marine Geology Frontiers, 35(10), Geng et al. The distribution and characteristics of mud volcanoes in the northeastern South China Sea.: 1–10, Copyright (2015), with permission from Science Press)

Zhang et al. 2020b). These features are characterized as chaotic, disrupted, blanking, pull-up, pull-down, and/or negative reflections on seismic and subbottom profiles (Fig. 3.9). These features are helpful for identifying the location and determining the formation mechanisms of gas seepages. High-angle faults, pipes, gas chimneys, and mud diapirs are usually good conduits for gas migration; they permits hydrocarbons to migrate from the deep strata to shallow strata and seep into the water column (Sun et al. 2012; Zhang et al. 2020b).

### 3.3 Quantitative Characterization of Gas Seepage

Quantitatively characterizations of gas seepage facilitate an understanding the fate and effect of gas seepage. The approaches for the estimation of gas seepage fluxes include acoustic methods (von Deimling et al. 2011; Li et al. 2020; Turco et al. 2022), chemical methods (Tryon and Brown 2004; Di et al. 2014; Leifer 2015), and optical methods (Römer et al. 2012; Wang et al. 2016; Higgs et al. 2019).

Optical methods usually rely on the manual and frame-by-frame analysis of the behavior and parameters of bubbles from video data acquired by a camera (Römer et al. 2012; Wang et al. 2016). Some semiautomatic and automatic analysis techniques



**Fig. 3.9** Gas migration pathway beneath the gas seepage station and bottom simulating reflection (BSR) at Site F in the northeastern South China Sea

have also been applied for bubble behavior and parameter measurements (Johansen et al. 2017; Higgs et al. 2019; Di et al. 2020; Veloso-Alarcón et al. 2022). However, most studies only show the behavior of single bubble streams and do not provide flow field images of gas seepages. Particle image velocimetry (PIV) technology is commonly used for visualizing fluid motion (Westerweel 2000; Adrian 2005). For example, Zhang et al. (2018) used PIV to image flow field of the hydrothermal plumes at mid-ocean ridge. Zhang et al. (2020c) and Li et al. (2021) tried to use PIV to image the flow field of cold seep in the SCS and Cascadia margin.

During the Deep-sea Exploration Shared Cruise (2019.4.10–2019.5.16, North-western South China Sea) with R/V Haiyang-6, a new and active cold seep (called “Haima 2019” in this chapter) was found approximately 50 km northeast of the “Haima” cold seeps (Geng et al. 2021). In situ video data from Haima 2019 were acquired using high-speed cameras mounted on the ROV Haima. The video data were converted to full resolution ( $1920 \times 1080$  pixels) images frame by frame using the open source software FFmpeg (<https://www.ffmpeg.org>). The pixel-to-mm parameter can be acquired separately for each image sequence according to a known reference measurement. After the conversion of pixels to mm, these high-resolution image sequences allow us to make detailed and accurate observations of gas seepage behaviors and parameters in Haima 2019 in the SCS.

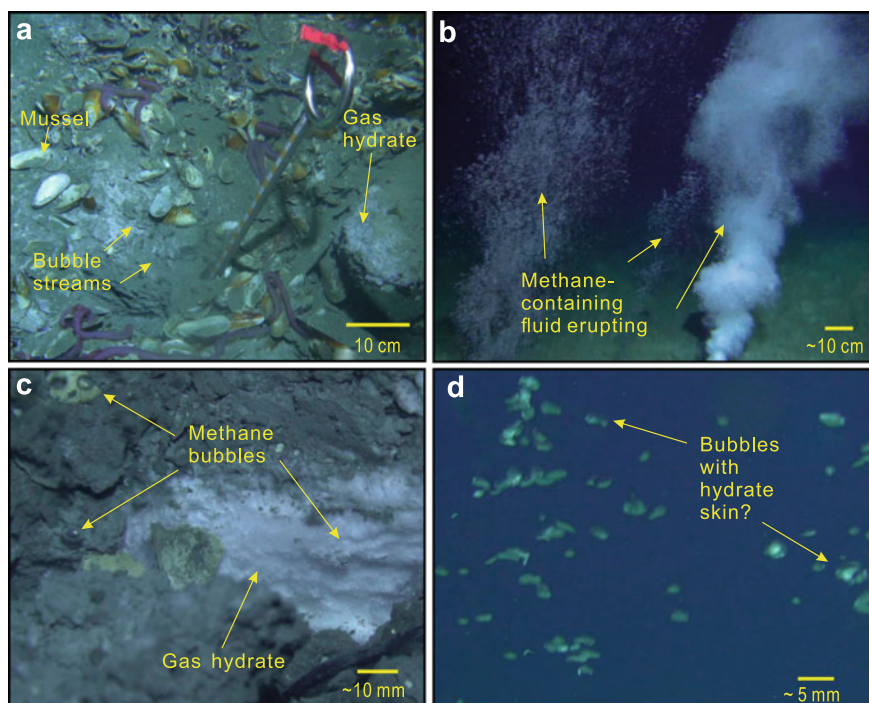
### 3.3.1 Manual Observations

According to the video image sequences, there were two types of gas seepages in Haima 2019 (Fig. 3.10). One consisted of gas bubbles, which were formed through gas hydrate decomposition and the slow escape of gas from the seafloor (seeping structure; Fig. 3.10a). The other was via plumes of gas-containing fluids, which erupted rapidly from the vent (erupting structure; Fig. 3.10b). As Fig. 3.10 shows,

there were some bubble streams near the seafloor, with abundant gas hydrate and cold seep biology, e.g., mussels (Fig. 3.10a) developed on the seafloor. The dissolved methane concentrations at Haima 2019 reached a value of 91 nmol/L, which is much higher than that of the normal bottom water (0.5–2.0 nmol/L, Di et al. 2020). It is speculated that most of the bubbles were methane bubbles formed through gas hydrate decomposition (Fig. 3.10c); these bubbles then slowly escaped from the seafloor and became methane bubble streams (Fig. 3.10a). As the bubbles rose, they became yellow and sheet-like (Fig. 3.10d). From this observation, we inferred that hydrate skins formed around the bubbles as they rose (Fig. 3.10d), in agreement with observations by Rehder et al. (2002) and Römer et al. (2012).

A gas-containing fluid rapidly erupted from the seafloor and formed three plumes (Fig. 3.10b). The plumes on the left and middle of this site are in gray, and the plume on the right is in white. The white particles in the plumes are inferred to be gas hydrates that erupted from the seafloor because of the high reservoir pressure in the study area (Wang et al. 2018a).

From the video observation, the average equivalent spherical bubble radius ( $r$ ) was estimated to be 2.924 mm. Thus, the average bubble volume, calculated as the mean



**Fig. 3.10** **a** Bubble streams seeping from the seafloor; **b** methane-containing fluid erupting from the seafloor; **c** gas hydrate decomposing and methane bubbles forming; **d** bubbles with hydrate skin. The scale of **(a)** is calculated according to the ruler in the image, while the **(b)**, **(c)**, and **(d)** is estimated according to experience point

of all individually estimated bubble volumes, was 0.128 ml. During an observation period of 2 min, the average bubble emission frequency was 12.34 bubbles/s. Using the average bubble emission frequency and the average bubble volume, a total bubble flux of approximately 94.8 ml/min for an individual bubble stream was calculated. The average rising velocity was 0.263 m/s, estimated from 23 bubbles within the size range of 2.556–4.624 mm in the upper region of the bubble streams.

### 3.3.2 PIV Observations

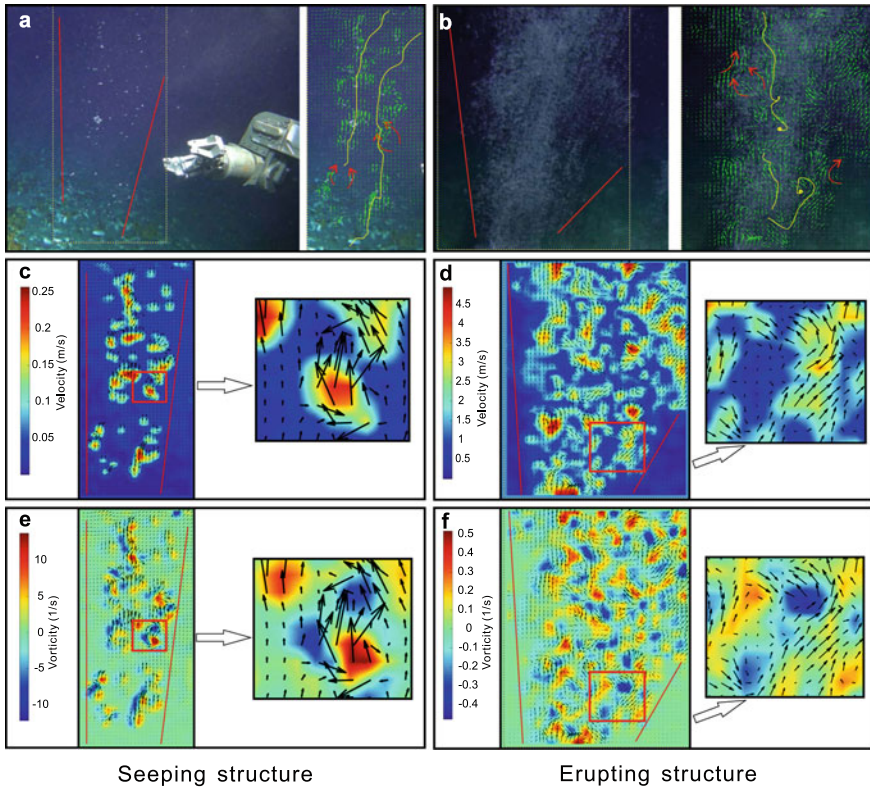
A GUI-based open-source tool (PIVlab) in MATLAB (MathWorks, Natick, Massachusetts) was used for PIV analyses of these gas seepage image sequences. The initial and final steps were  $64 \times 64$  pixels and  $32 \times 32$  pixels, or  $48 \times 48$  pixels and  $24 \times 24$  pixels, respectively, with an overlap of 50%. After the velocity field was acquired, the vorticity ( $\omega$ ) was also calculated according to the curl of the velocity. More detailed information can be found in Thielicke and Stamhuis (2014).

As the vector field images show (Fig. 3.11a and b), both the outlines of the seeping structure (Fig. 3.11a) and erupting structure (Fig. 3.11b) flow field had a plume structure, which is smaller at the bottom and gradually enlarges upward. The plume boundaries were easier to identify in velocity field images (Fig. 3.11c). The streamlines of the cold seep flow were zigzags, which indicated that the bubbles and other fluids did not rise vertically (Fig. 3.11a and b). The velocity magnitude was higher at the center region of the plume and gradually decreased to almost zero at the boundary region of the plume (Fig. 3.11c and d). Many high-velocity magnitude points are present in the velocity field of the bubble streams (Fig. 3.11c). These points can be considered methane bubbles, and the velocity decreased with distance from the core of the bubbles (Gong et al. 2009). Thus, we obtained not only the single rise velocity of the bubbles but also the velocity of the bubble-induced flow. Turbulent motion is visible within the flow field images (Fig. 3.11), and they are more distinct in the velocity field (Fig. 3.11c and d) and vorticity field (Fig. 3.11e and f). At the edge of the plumes, seawater was carried into the plumes by the turbulent eddies, which may have been responsible for the upward enlargement of the plumes (Fig. 3.11d). Within the plumes, the turbulent eddies were more developed (Fig. 3.11e and f).

These results also provide quantitative information on the cold seep flow field. The seeping velocity flow field ranged from 0 to 0.337 m/s, while the erupting velocity flow field ranged from 0 to approximately 6.461 m/s. The maximum velocity of the erupting structure was approximately 19 times larger than the maximum velocity of the seeping structures. The vorticity of the seeping structure ranged from  $-27.073$  to  $20.394$  1/s. The vorticity of the erupting structure ranged from  $-809.324$  to  $910.307$  1/s. The quantitative results also showed that the vorticity of the erupting structure was much larger than that of the seeping structure.

Figure 3.12a and b show velocity field changes. The velocity field change in Fig. 3.12b was recorded 0.0334 s after that in Fig. 3.12a. It is clear that the velocity field changed, even within this short time interval. Both the direction and velocity of

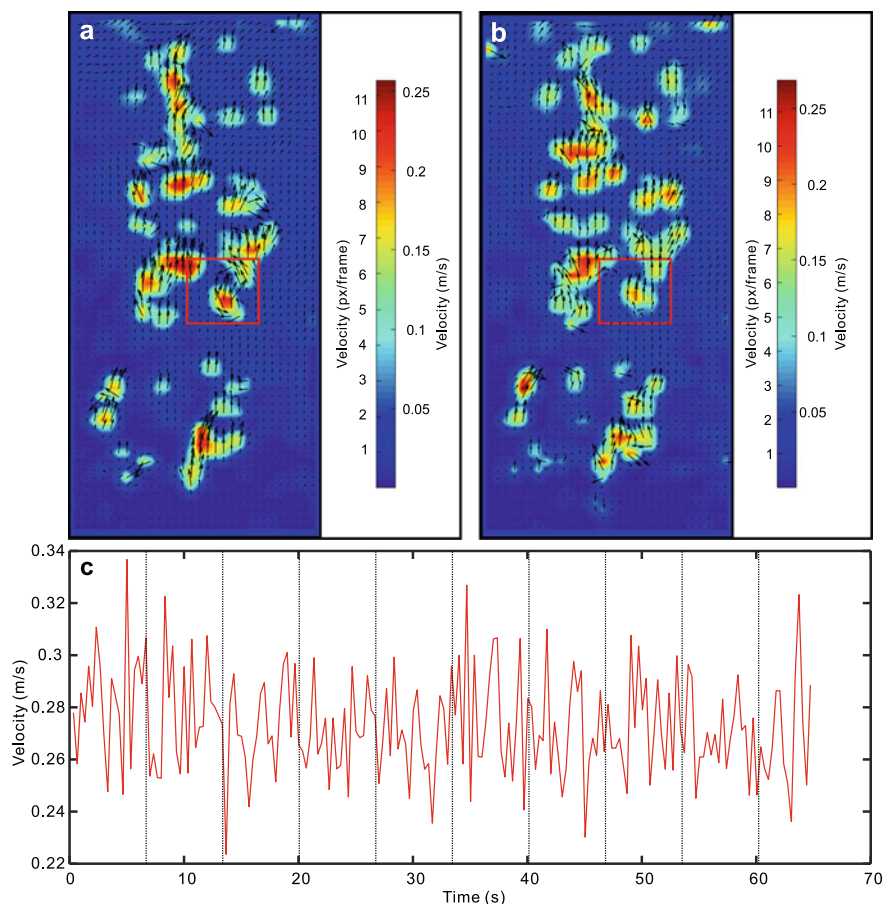




**Fig. 3.11** Images of the cold seep flow field. **a** Original (left) and vector (right) images of the seeping structure; **b** original (left) and vector (right) images of the erupting structure; **c** velocity field of the seeping structure; **d** velocity field of the erupting structure; **e** vorticity image of the seeping structure; **f** vorticity image of the erupting structure. The red lines show the boundaries of the cold seep flow. The streams are indicated by yellow lines

the cold seep flow changed with time (Fig. 3.12a and b). For example, the velocity field direction changed from the upper right to vertically upward in the red box region of Fig. 3.12a and b. In addition, the velocity values became slightly lower. The time-dependent variations in maximum velocity are mapped in Fig. 3.12c. A short-period cycle of 6.6 s was observed (Fig. 3.12c), which is far shorter than the general tidal cycle (~24 h) of cold seeps (Römer et al. 2016).

These results show that the PIV method is a feasible and powerful tool to visualize cold seep flow properties within the water column. It is a nonintrusive measurement with high sampling frequency and can show overall changes in field images, not simply individual static values. Regarding the possibilities for the use of PIV in cold seep systems, it can be stated that the images of cold seep flow fields provide a new approach for observing cold seep flows, and the scope of their future research applications is broad.



**Fig. 3.12** Temporal variations in the cold seep flow field. **a** Velocity field of frame 1152; **b** velocity field of frame 1153; **c** time series of velocity

### 3.4 Gas Migration Mechanisms

Overpressure is a fundamental condition for gas migration and seepage. However, differences in gas sources, conduit systems and patterns induce different gas migration mechanisms in different regions of the SCS. At Site F, continuous and strong BSRs, sediment waves, mass transport deposits, and gas chimneys were discovered in seismic profiles (Hsu et al. 2018b; Wang et al. 2018b). Methane-rich fluids present inside sediment ridges migrated upward along gas chimneys and other conduits, and sulfate carried by cold seawater flowed into the fluid systems from both flanks of the sediment ridge, and this formed the gas seepages at Site F.

For the Haima cold seep area and Haima 2019 in the Qiongdongnan Basin, polarity reverses, pull-downs, deep faults, minor faults, gas chimneys, and BSRs were also

discovered in the seismic profiles (Wei et al. 2020; Geng et al. 2021). The gas seepages showed spatiotemporal variations, which are controlled by the gas migration process from the deep strata to the seafloor. The gas migration originating from the deep reservoir migrates along the deep faults, the slope of the basal uplift, and the gas chimney to the shallow sediments. Gas accumulated at shallow depths forms gas hydrates and increases pore pressure. When the pore pressure overcomes the overburdened sediment, fractures are generated for gas migration to the water column. Gas emission and eruption decrease the pressure in the shallow sediments, which stops the fractures from reaching the seafloor. However, gas seepage along the fractures might cease with gas hydrate development and authigenic carbonate precipitation, which decreases the permeability of the original fractures. Consequently, pressure rebuilds in the shallow sediments, and new fractures are generated.

However, most gas migration mechanism studies in the SCS are limited to isolated stations. Comparison and holistic studies are needed to summarize the gas migration mechanisms in the SCS in the future. Physical and numerical simulations of the gas migration process are scarce in the SCS. The relationships between gas seepage and geohazards, e.g., submarine landslides and tsunamis, also need to be studied in the future.

### 3.5 Summary and Perspectives

Gas seepage is characterized as bubble plumes in water, which can be detected by several kinds of acoustic devices and optical investigations. The formation and evolution of gas seepages can alter the seafloor and produce various kinds of features on and below the seafloor, e.g., chemosynthetic communities, authigenic carbonate, pockmarks, and mud volcanoes on the seafloor, and BSRs, gas chimneys, high-angle faults, pipes, and polarity reversals in the subsurface layers. These features have unique manifestations in topographical data, seismic data, sidescan sonar data, and subbottom data.

The research on gas seepages has gradually shifted from qualitative descriptions to quantitative characterizations. Generally, the parameters for gas seepages are estimated according to manual observation or acoustic devices. A nonintrusive measurement, called the PIV method, conducted with a high sampling frequency optical device is introduced in this chapter and provides a new approach to study gas seepages quantitatively. Gas migration mechanisms are discussed in this chapter. Overpressure in marine sediments is a significant gas transport mechanism. The subsurface structures, e.g., faults, gas chimneys, pipes, and other conduits, also influence gas migration.

With the development of research equipment and underwater positioning and navigation systems, the comprehensive detection of gas seepages has become feasible, which can help us understand the formation and mechanism of gas seepages further.



Long-term, three-dimensional, and comprehensive observations are needed to quantitatively characterize gas seepages. Physical and numerical simulations of gas migration and hazard processes could also facilitate understanding of the fate of gas seepages in the future.

**Acknowledgements** We thank the Guangzhou Marine Geological Survey for releasing these data for scientific research. Mr. Yongxian Guan and Dr. Baojin Zhang are thanked for their kind help and support during our visit in Guangzhou.

## References

- Adrian RJ (2005) Twenty years of particle image velocimetry. *Exp Fluids* 39(2):159–169
- Bai Y, Song H, Guan Y et al (2014) Structural characteristics and genesis of pockmarks in the Northwest of the South China Sea derived from reflective seismic and multibeam data. *Chinese J Geophys-Chinese Ed* 57(7):2208–2222 (in Chinese with English abstract)
- Ceramicola S, Dupré S, Somoza L et al (2018) Cold seep systems. In: Micallef A, Krastel S, Savini A (eds) *Submarine Geomorphology*. Springer International Publishing, Cham, pp 367–387
- Chen L, Song H (2005) Geophysical features and identification of natural gas seepage in marine environment. *Prog Geophys* 20(4):1067–1073 (in Chinese with English abstract)
- Chen SC, Hsu SK, Tsai CH et al (2010) Gas seepage, pockmarks and mud volcanoes in the near shore of SW Taiwan. *Mar Geophys Res* 31(1–2):133–147
- Chen J, Guan Y, Song H et al (2015a) Distribution characteristics and geological implications of pockmarks and mud volcanoes in the northern and western continental margins of the South China Sea. *Chinese J Geophys-Chinese Ed* 58(3):919–938 (in Chinese with English abstract)
- Chen J, Song H, Guan Y et al (2015b) Morphologies, classification and genesis of pockmarks, mud volcanoes and associated fluid escape features in the northern Zhongjiannan Basin, South China Sea. *Deep-Sea Res Part II-Top Stud Oceanogr* 122:106–117
- Chen J, Song H, Guan Y et al (2017) A preliminary study of submarine cold seeps by seismic oceanography techniques. *Chinese J Geophys-Chinese Ed* 60(1):117–129
- Chen J, Tong S, Han T et al (2020) Modelling and detection of submarine bubble plumes using seismic oceanography. *J Mar Syst* 209(103375):1–11
- Dandapath S, Chakraborty B, Karisiddaiah SM et al (2010) Morphology of pockmarks along the western continental margin of India: employing multibeam bathymetry and backscatter data. *Mar Pet Geol* 27(10):2107–2117
- Di P, Huang H, Huang B et al (2012) Seabed pockmark formation associated with mud diapir development and fluid activities in the Yinggehai Basin of the South China Sea. *J Trop Oceanogr* 31(5):26–36 (in Chinese with English abstract)
- Di P, Feng D, Chen D (2014) In-situ and on-line measurement of gas flux at a hydrocarbon seep from the northern South China Sea. *Cont Shelf Res* 81:80–87
- Di P, Feng D, Tao J et al (2020) Using time-series videos to quantify methane bubbles flux from natural cold seeps in the South China Sea. *Minerals* 10(3):1–17
- Dumke I, Klauke I, Berndt C et al (2014) Sidescan backscatter variations of cold seeps on the Hikurangi margin (New Zealand): indications for different stages in seep development. *Geo-Mar Lett* 34(2–3):169–184
- Dupré S, Buffet G, Mascle J et al (2008) High-resolution mapping of large gas emitting mud volcanoes on the Egyptian continental margin (Nile Deep Sea Fan) by AUV surveys. *Mar Geophys Res* 29(4):275–290
- Feng D, Chen D, Peckmann J et al (2010) Authigenic carbonates from methane seeps of the northern Congo Fan: microbial formation mechanism. *Mar Pet Geol* 27(4):748–756

- Feng D, Qiu JW, Hu Y et al (2018) Cold seep systems in the South China Sea: an overview. *J Asian Earth Sci* 168:3–16
- Gay A, Lopez M, Cochonat P et al (2006) Isolated seafloor pockmarks linked to BSRs, fluid chimneys, polygonal faults and stacked Oligocene-Miocene turbiditic palaeochannels in the Lower Congo Basin. *Mar Geol* 226(1–2):25–40
- Geng M, Song H, Guang Y et al (2019) The distribution and characteristics of mud volcanoes in the northeastern South China Sea. *Mar Geol Front* 35(10):1–10 (in Chinese with English abstract)
- Geng M, Zhang R, Yang S et al (2021) Focused fluid flow, shallow gas hydrate, and cold seep in the Qiongdongnan Basin, northwestern South China Sea. *Geofluids* 2021:1–11
- Gong X, Takagi S, Matsumoto Y (2009) The effect of bubble-induced liquid flow on mass transfer in bubble plumes. *Int J Multiph Flow* 35(2):155–162
- He J, Zhu Y, Weng R et al (2010) Characters of north-west mud diapirs volcanoes in South China Sea and relationship between them and accumulation and migration of oil and gas. *Earth Sci* 35(1):75–86 (in Chinese with English abstract)
- Higgs B, Mountjoy J, Crutchley GJ et al (2019) Seep-bubble characteristics and gas flow rates from a shallow-water, high-density seep field on the shelf-to-slope transition of the Hikurangi subduction margin. *Mar Geol* 417:105985
- Hovland M, Heggland R, De Vries MH et al (2010) Unit-pockmarks and their potential significance for predicting fluid flow. *Mar Pet Geol* 27(6):1190–1199
- Hsu SK, Wang SY, Liao YC et al (2013) Tide-modulated gas emissions and tremors off SW Taiwan. *Earth Planet Sci Lett* 369–370:98–107
- Hsu HH, Liu CS, Morita S et al (2018a) Seismic imaging of the Formosa Ridge cold seep site offshore of southwestern Taiwan. *Mar Geophys Res* 39(4):523–535
- Hsu SK, Lin SS, Wang SY et al (2018b) Seabed gas emissions and submarine landslides off SW Taiwan. *Terr, Atmos Ocean Sci* 29(1):7–15
- Johansen C, Todd AC, MacDonald IR (2017) Time series video analysis of bubble release processes at natural hydrocarbon seeps in the Northern Gulf of Mexico. *Mar Pet Geol* 82:21–34
- Judd A, Hovland M (2007) Seabed fluid flow: the impact on geology, biology and the marine environment. Cambridge University Press, New York. <https://doi.org/10.5860/choice.45-0294>
- Kvenvolden KA (1993) Gas hydrates-geological perspective and global change. *Rev Geophys* 31(2):173–187
- Leifer I (2015) Seabed bubble flux estimation by calibrated video survey for a large blowout seep in the North Sea. *Mar Pet Geol* 68:743–752
- Li HJ, Song HB, Zhang K et al (2021) A quantitative study on the active cold seep flow field along the Cascadia margin. *Chinese J Geophys-Chinese Ed* 64(8):2982–2993 (in Chinese with English abstract)
- Li J, Roche B, Bull JM et al (2020) Broadband acoustic inversion for gas flux quantification. Appl a methane plume Scanner pockmark, Cent. North Sea. *J Geophys Res-Oceans* 125(9):e2020JC016360
- Liu B (2017) Gas and gas hydrate distribution around seafloor mound in the Dongsha area, north slope of the South China Sea. *Haiyang Xuebao* 39(3):68–75 (in Chinese with English abstract)
- Liu B, Song H, Guan Y et al (2015) Characteristics and formation mechanism of cold seep system in the northeastern continental slope of South China Sea from sub-bottom profiler data. *Chinese J Geophys-Chinese Ed* 58(1):247–256 (in Chinese with English abstract)
- Liu B, Chen J, Yang L et al (2021) Multi-beam and seismic investigations of the active Haima cold seeps, northwestern South China Sea. *Acta Oceanol Sin* 40(7):183–197
- Luo M, Dale AW, Wallmann K et al (2015) Estimating the time of pockmark formation in the SW Xisha Uplift (South China Sea) using reaction-transport modeling. *Mar Geol* 364:21–31
- Pilcher R, Argent J (2007) Mega-pockmarks and linear pockmark trains on the West African continental margin. *Mar Geol* 244(1–4):15–32
- Rehder G, Brewer PW, Peltzer ET et al (2002) Enhanced lifetime of methane bubble streams within the deep ocean. *Geophys Res Lett* 29(15):1–4

- Römer M, Sahling H, Pape T et al (2012) Quantification of gas bubble emissions from submarine hydrocarbon seeps at the Makran continental margin (offshore Pakistan). *J Geophys Res-Oceans* 117(C10):1–19
- Römer M, Riedel M, Scherwath M et al (2016) Tidally controlled gas bubble emissions: A comprehensive study using long-term monitoring data from the NEPTUNE cabled observatory offshore Vancouver Island. *Geochem Geophys Geosyst* 17(9):3797–3814
- Schroot BM, Klaver GT, Schüttenhelm RTE (2005) Surface and subsurface expressions of gas seepage to the seabed - examples from the Southern North Sea. *Mar Pet Geol* 22(4):499–515
- Sultan N, Bohrmann G, Ruffine L et al (2014) Pockmark formation and evolution in deep water Nigeria: Rapid hydrate growth versus slow hydrate dissolution. *J Geophys Res-Solid Earth* 119(4):2679–2694
- Sun Q, Wu S, Hovland M et al (2011) The morphologies and genesis of mega-pockmarks near the Xisha Uplift, South China Sea. *Mar Pet Geol* 28(6):1146–1156
- Sun Q, Wu S, Cartwright J et al (2012) Shallow gas and focused fluid flow systems in the Pearl River Mouth Basin, northern South China Sea. *Mar Geol* 315–318:1–14
- Sun Q, Wu S, Cartwright J et al (2013) Focused fluid flow systems of the Zhongjiannan Basin and Guangle Uplift South China Sea. *Basin Res* 25(1):97–111
- Talukder AR (2012) Review of submarine cold seep plumbing systems: leakage to seepage and venting. *Terr Nova* 24(4):255–272
- Thielicke W, Stamhuis EJ (2014) PIVlab – towards user-friendly, affordable and accurate digital particle image velocimetry in MATLAB. *J Open Res Software* 2(e30):1–10
- Tryon MD, Brown KM (2004) Fluid and chemical cycling at Bush Hill: implications for gas- and hydrate-rich environments. *Geochem Geophys Geosyst* 5(12):1–7
- Turco F, Lacroix Y, Watson SJ et al (2022) Estimates of methane release from gas seeps at the southern Hikurangi margin New Zealand. *Front Earth Sci* 10(834047):1–20
- Urban P, Köser K, Greinert J (2017) Processing of multibeam water column image data for automated bubble/seep detection and repeated mapping. *Limnol Oceanogr Meth* 15:1–21
- Veloso-Alarcón ME, Urban P, Weiss T et al (2022) Quantitatively monitoring bubble-flow at a seep site offshore Oregon: Field trials and methodological advances for parallel optical and hydroacoustical measurements. *Front Earth Sci* 10(858992):1–23
- von Deimling JS, Rehder G, Greinert J et al (2011) Quantification of seep-related methane gas emissions at Tommeliten North Sea. *Cont Shelf Res* 31(7–8):867–878
- Wan Z, Yao Y, Chen K et al (2019) Characterization of mud volcanoes in the northern Zhongjiannan Basin, western South China Sea. *Geol J* 54(1):177–189
- Wang B, Socolofsky SA, Breier JA et al (2016) Observations of bubbles in natural seep flares at MC 118 and GC 600 using in situ quantitative imaging. *J Geophys Res-Oceans* 121(4):2203–2230
- Wang J, Wu S, Kong X et al (2018a) Subsurface fluid flow at an active cold seep area in the Qiongdongnan Basin, northern South China Sea. *J Asian Earth Sci* 168:17–26
- Wang X, Liu B, Qian J et al (2018b) Geophysical evidence for gas hydrate accumulation related to methane seepage in the Taixinan Basin, South China Sea. *J Asian Earth Sci* 168:27–37
- Wang LJ, Zhu JT, Zhuo HT et al (2019) Seismic characteristics and mechanism of fluid flow structures in the central depression of Qiongdongnan Basin, northern margin of South China Sea. *Int Geol Rev* 62(7–8):1108–1130
- Wang B, Du Z, Luan Z et al (2021) Seabed features associated with cold seep activity at the Formosa Ridge, South China Sea: Integrated application of high-resolution acoustic data and photomosaic images. *Deep-Sea Res Part I-Oceanogr Res Pap* 177(2021):103622
- Wei J, Li J, Wu T et al (2020) Geologically controlled intermittent gas eruption and its impact on bottom water temperature and chemosynthetic communities—A case study in the “HaiMa” cold seeps South China Sea. *Geol J* 55(9):6066–6078
- Westerweel J (2000) Theoretical analysis of the measurement precision in particle image velocimetry. *Exp Fluids* 29(7):S003-S012
- Xu H, Xing T, Wang J et al (2012) Detecting seepage hydrate reservoir using multi-channel seismic reflecting data in Shenhu area. *Earth Sci* 37(S1):195–202 (in Chinese with English abstract)

- Yang L, Liu B, Xu M et al (2018) Characteristics of active cold seepages in Qiongdongnan Sea Area of the northern South China Sea. *Chinese J Geophys-Chinese Ed* 61(7):2905–2914 (in Chinese with English abstract)
- Yu K, Miramontes E, Alves TM et al (2021) Incision of submarine channels over pockmark trains in the South China Sea. *Geophys Res Lett* 48(e2021GL092861):1–13
- Zhang X, Lin J, Jiang H (2018) Time-dependent variations in vertical fluxes of hydrothermal plumes at mid-ocean ridges. *Mar Geophys Res* 40:245–260
- Zhang T, Wu Z, Zhao D et al (2019) The morphologies and genesis of pockmarks in the Reed Basin South China Sea. *Haiyang Xuebao* 41(3):106–120 (in Chinese with English abstract)
- Zhang K, Guan Y, Song H et al (2020a) A preliminary study on morphology and genesis of giant and mega pockmarks near Andu Seamount, Nansha Region (South China Sea). *Mar Geophys Res* 41(2):1–12
- Zhang K, Song H, Wang H et al (2020b) A preliminary study on the active cold seeps flow field in the Qiongdongnan Sea Area, the northern South China Sea. *Chin Sci Bull* 65(12):1130–1140 (in Chinese with English abstract)
- Zhang W, Liang J, Yang X et al (2020c) The formation mechanism of mud diapirs and gas chimneys and their relationship with natural gas hydrates: insights from the deep-water area of Qiongdongnan Basin, northern South China Sea. *Int Geol Rev* 62(7–8):789–810
- Zhu C, Cheng S, Zhang M et al (2018) Results from Multibeam Survey of the Gas Hydrate Reservoir in the Zhujiang Submarine Canyons. *Acta Geol Sin-Engl Ed* 92(2):135–138
- Zhu S, Li X, Zhang H et al (2020) Types, characteristics, distribution, and genesis of pockmarks in the South China Sea: insights from high-resolution multibeam bathymetric and multichannel seismic data. *Int Geol Rev* 63(12):1682–1702

**Open Access** This chapter is licensed under the terms of the Creative Commons Attribution 4.0 International License (<http://creativecommons.org/licenses/by/4.0/>), which permits use, sharing, adaptation, distribution and reproduction in any medium or format, as long as you give appropriate credit to the original author(s) and the source, provide a link to the Creative Commons license and indicate if changes were made.

The images or other third party material in this chapter are included in the chapter's Creative Commons license, unless indicated otherwise in a credit line to the material. If material is not included in the chapter's Creative Commons license and your intended use is not permitted by statutory regulation or exceeds the permitted use, you will need to obtain permission directly from the copyright holder.

